# Selection of the numerical formulation for modeling the effect of tool cutting edge microgeometries in machining of Ti6Al4V titanium alloy

Cheng Hu [a,b], José Outeiro [a,c,*], Kejia Zhuang [b,**], Hélène Birembaux [a]

[a] LaBoMaP, Arts et Métiers Institute of Technology Campus of Cluny, Cluny 71250, France
[b] Hubei Digital Manufacturing Key Laboratory, School of Mechanical and Electronic Engineering, Wuhan University of Technology, Wuhan 430070, China
[c] Department of Mechanical Engineering and Engineering Science, University of North Carolina at Charlotte, Charlotte, NC 28223, United States

*Keywords:*
Metal cutting
Tool cutting edge microgeometry
Modeling
Numerical formulation
Finite element method
Constitutive model

A B S T R A C T

The Finite-element method (FEM) is often used to simulate the metal machining process. Currently, several formulations are used in metal cutting simulation, such as Lagrangian (LAG), Eulerian (EUL), Arbitrary Lagrangian–Eulerian (ALE), and Coupled Eulerian–Lagrangian (CEL). The selection of the numerical formulation that better reproduces the material separation in machining to form the chip is a critical issue. This is quite important when the ratio between the uncut chip thickness and the cutting edge microgeometry, often represented by a cutting edge radius, is very low. In this study, orthogonal cutting of Ti6Al4V titanium alloy using different tool edge microgeometries is investigated using LAG and CEL approaches. In the case of LAG approach, two types of cutting models were develop: one using a sacrificial layer (hereby called LAG-SL), and another without sacrificial layer (hereby called LAG-nSL). The cutting models have included a constitutive model (both plasticity and damage) considering the effects of strain, strain rate, temperature, and state of stress, which have proved to be accurate enough to represent the mechanical behavior of the Ti6Al4V alloy in machining. Comprehensive comparisons between CEL and LAG-based cutting models and experimental results are carried out in terms of chip morphology, forces, and residual stresses. When compared to the experimental results, LAG-nSL model gives the best predictions of the maximum chip compression ratio ($CCR_m$) with an error of 9.5%, cutting force (12.8%) and thrust force (9.3%) than the other two models. In the case of the of residual stress profiles, LAG-SL offers good predictions of the maximum compressive residual stress by a preference ratio of 75%. Although CEL yields the worst predictions of chip morphology and forces, it is preferred from the perspective of the thickness of the layer affected by residual stress.

* Corresponding author at: Department of Mechanical Engineering and Engineering Science, University of North Carolina at Charlotte, Charlotte, NC 28223, United States.
** Corresponding author.
*E-mail addresses:* jc.outeiro@charlotte.edu (J. Outeiro), zhuangkj@whut.edu.cn (K. Zhuang).

https://doi.org/10.1016/j.simpat.2023.102816

## 1. Introduction

The growing demand on high-quality machined parts for aerospace industry made on superalloys like the Ti6Al4V titanium alloy have gained much attention from researchers worldwide. Metal cutting is characterized by strong gradients of strain, strain rate, stress, and temperature. Moreover, they are time-dependent (cyclic variation) and locate near the tool cutting edge, representing a challenge to accurately capture them experimentally. Therefore, to analyze these gradients of process variables in the vicinity of the cutting edge, numerical methods, in particular the finite-element method (FEM), are widely adopted, due to the improvements of the computational power. Therefore, the studies on the cutting process have still been benefitting enormously from the numerical simulation, regarding its computational accuracy [1]. The numerical simulation using FEM can not only predict these process variables but also their effects on the machining process, such as material flow [2], chip morphology [3], surface integrity (surface roughness [4], microstructure evolution [5], and residual stress [6]). However, this great improvements on the numerical simulation are not accompanied by a better understanding of the metal cutting process physics [7], and consequently the cutting models still need to be improved in order to accurately represent the reality.

To develop cutting models for metal machining process, several numerical formulations have been frequently used, including Lagrangian (LAG), Eulerian (EUL), Arbitrary Lagrangian–Eulerian (ALE), and Coupled Eulerian-Lagrangian (CEL) [8,9]. Usually, one or several of these formulations are already built-in commercial FE packages like Abaqus [10], Deform [11] and Third Wave AdvantEdge [12]. Effects of different formulations on the cutting process variables can be found in many scientific publications. Among these, chip morphology is the most direct reflection of the difference amidst these formulations. Soliman et al. [13] compared LAG and ALE in the cutting simulation of AISI 1045 steel. To be able to better simulate the material separation to form the chip, a thin sacrificial layer (SL) with very low damage threshold was added between the uncut chip layer and the remained part of the workpiece, which is hereby called LAG-SL. They observed that both formulations permitted to obtain an accurate prediction of the average forces. Concerning to the chip morphology, ALE formulation produced a continuous chip while LAG produced a segmented one. To obtain segmented chips in simulating cutting of A2024–T351 alloy, Zhang and Choi [3] employed LAG-SL, ALE with and without SL as well as CEL with coarse and fine meshes. They concluded that LAG-SL had the advantage in simulating adiabatic shear failure while ALE and CEL did not. Similar results were obtained by Zhang et al. [14] who used cutting models including two sets of coefficients of Johnson–Cook (J–C) constitutive model and three numerical formulations (LAG-SL, ALE, CEL). They found that the chip segmentation occurs only with LAG-SL. However, Xu et al. [15] simulated the orthogonal cutting of Ti6Al4V alloy using LAG-SL and CEL formulations. They concluded that CEL formulation can give also serrated chip and it predicted better the strains and chip-tool contact length than LAG-SL which showed apparent element distortions on both chip-tool interface and machined surface. This is related to the different chip separation criteria, which for CEL and ALE is node-splitting technique while for LAG-SL is element deletion technique [16].

The change of numerical formulation could also lead to noticeable difference in forces. Ducobu et al. [17] studied the simulation of orthogonal cutting of Ti6Al4V alloy using three combinations of numerical formulations (ALE and LAG-SL) and constitutive models (TANH law with and without crack propagation). They found the combination of LAG-SL with TANH model with crack propagation could give satisfactory chip serration, but it showed a reduction of 33% in simulated thrust forces. They pointed out the influence of tool cutting edge radius was not well considered when using LAG-SL model. In their later study [18], an overestimation difference up to 176% was attained in evaluating the simulated thrust force by applying the LAG-SL model to machining Ti6Al4V with different cutting widths. Such difference could be attributed to the improper definition of SL as well as the constitutive damage model. Yameogo et al. [19] who obtained a cutting force of 238N using LAG-SL with J–C damage constitutive model while the experimental measurement was 386 $\pm$ 1N. Cheng and Outeiro [20] also reported that a model using LAG-SL could lead to significant underestimation up to 52% of thrust force in orthogonal cutting of Ti6Al4V, even though the cutting force and chip morphology were in good agreement with the experimental observations. Silva and Outeiro [21] utilized LAG-SL and CEL to simulate the orthogonal cutting of Inconel 718 alloy. They found the forces using CEL showed good agreement with the measurements while LAG-SL showed an underestimation error near 52%.

As for residual stress calculation, Silva and Outeiro [21] came to the conclusion that LAG-SL model yielded better simulations than CEL. Besides, from machined surface to 30 μm below it, noticeable overestimations were found using CEL for of residual stresses in both cutting and perpendicular to cutting directions. In the results presented by Cheng and Outeiro [20] using LAG-SL model, the predicted residual stresses before 20 μm below the machined surface were found significantly different from the experimental ones. Similar results were obtained by Rotella and Umbrello [22] when simulating the machining of Ti6Al4V alloy under dry and cryogenic cooling conditions.

The above presented studies show that the numerical formulations can significantly affect the machining process variables, including the chip geometry, forces and residual stress. This stems mainly from their discrepancies in characterizing the work material flow around the cutting edge, which affects directly both the formation of chip and machined surface [23]. However, the severe element distortion problem will interrupt the calculation when adopting LAG-SL [17], especially for the model considering tool cutting edge microgeometry. On the one hand, increasing the thickness of SL to cover the cutting edge may solve this problem but it will lead to worse outcomes of forces and residual stress as aforementioned. On the other hand, one may resort to ALE and CEL, but non-of them could yield the adiabatic shear band and crack propagation [24], which are typical in machining titanium alloy. Therefore, for better understanding and wider application, a comprehensive evaluation and improvement on current numerical formulations concerning

tool cutting edge microgeometry is still necessary.

In this paper three orthogonal cutting models using each one different numerical formulation (CEL, LAG-SL, and LAG without SL, hereby denoted by LAG-nSL) were developed and applied to evaluate the influence of each formulation, and to investigate the effect of the tool edge microgeometry on the chip morphology, forces, and residual stresses. These cutting models have included a constitutive model (both plasticity and damage) considering the effects of strain, strain rate, temperature, and state of stress, which has been proved to be accurate enough to represent the mechanical behaviors of the Ti6Al4V alloy in machining [15,20]. This constitutive model was implemented in Abaqus FEA software code through a user-defined subroutine VUMAT. A series of simulations using these three orthogonal cutting models were carried out by varying the cutting speed, uncut chip thickness (UCT) and tool cutting edge radius. Finally, a comprehensive evaluation was performed to evaluate the accuracy of these three cutting models to predict the chip morphology, forces, and residual stresses.

## 2. Constitutive model and its implementation in FE code

### 2.1. Constitutive model description

To obtain an accurate prediction of the deformation process in metal cutting, the constitutive models including both the plasticity and damage are of great significance. Among the prevailing constitutive models, Johnson–Cook (J–C) plasticity and damage expressions are most widely applied to metal cutting process due to it relatively simplicity to represent the effects of the strain, plastic strain rate, and temperature on the mechanical behavior of the work material. As formulated by Eqs. (1)–(3), Xu et al. [15] modified J–C models based on the work of Bai and Wierzibicki [25] and Cheng et al. [26], who considered additionally the effect of the state of stress (SoT).

$$\sigma_y = \left(A + m\left(\varepsilon_p\right)^{\mathrm{n}}\right)\left(B + C\cdot \mathrm{In}\left(E + \frac{\dot{\varepsilon}_p}{\dot{\varepsilon}_0}\right)\right)\left(1 - \left(\frac{T - T_0}{T_m - T_0}\right)^{t}\right) \times (1 - c_\eta(\eta - \eta_0))\left(c_\theta^s + \left(c_\theta^{ax} - c_\theta^s\right)\left(\gamma - \frac{\gamma^{a+1}}{a+1}\right)\right) \tag{1}$$

$$\gamma = 6.464(\sec(\overline{\theta}\cdot\pi/6) - 1) \tag{2}$$

$$c_\theta^{ax} = \begin{cases} c_\theta^t & (\overline{\theta} > 0) \\ c_\theta^c & (\overline{\theta} \le 0) \end{cases} \tag{3}$$

In Eq. (1), $A$, $B$, $C$, $E$, $n$, $m$ and $t$ are coefficients concerning the strain hardening, strain rate effects and thermal softening of the workpiece material, which are often determined based on mechanical testing. The variables $\varepsilon_p$, $\dot{\varepsilon}_p$, $T$ stand for the plastic strain, plastic strain rate, and temperature at the integration points. $c_\eta$, $c_\theta^s$, $c_\theta^t$, $c_\theta^c$, $c_\theta^{ax}$ are coefficients related to the state of stress. The other three coefficients, $\varepsilon_0$, $\eta_0$, $T_m$ and $T_0$, are respectively, the reference strain rate, reference stress triaxiality, melting temperature, and the room temperature. The parameters $\eta$ and $\overline{\theta}$ in Eq. (2) are the stress triaxiality and normalized Lode angle parameter, respectively. They are used to describe the state of stress, and given by the following equation:

$$\begin{cases} \eta = -p/q = \sigma_m/\overline{\sigma} \\ \xi = (r/q)^3 = \cos(3\theta) \\ \overline{\theta} = 1 - 6\theta/\pi = 1 - (2/\pi)\arccos(\xi) \end{cases} \tag{4}$$

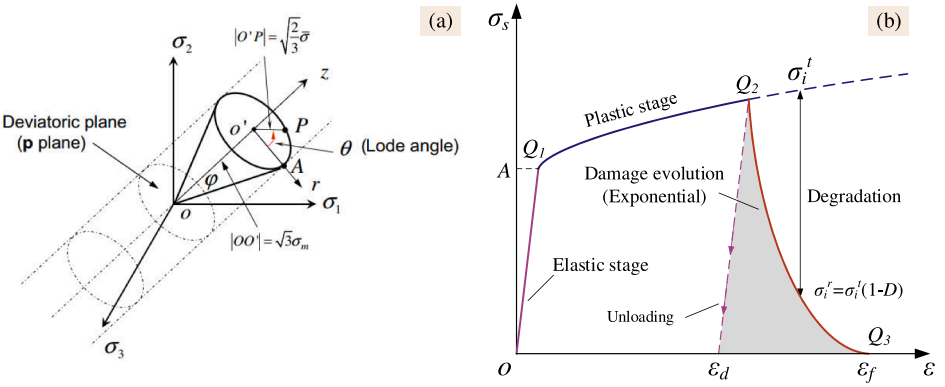


**Fig. 1.** Schematic representation of (a) state of principal stresses and (b) stress-strain curve.

It can be found from Eq. (4) that the normalized Lode parameter $\theta$ is ranging within [−1, 1]. The variable $p$, $q$ and $r$ stand for the three invariants of deviatoric stress tensor, which can be calculated with the following equations:

$$\begin{cases} p = -\sigma_m = -\dfrac{1}{3}(\sigma_1 + \sigma_2 + \sigma_2) \\ q = \overline{\sigma} = \sqrt{\dfrac{3}{2}\mathbf{S} : \mathbf{S}} = \sqrt{\dfrac{1}{2}\left((\sigma_1 - \sigma_2)^2 + (\sigma_2 - \sigma_3)^2 + (\sigma_3 - \sigma_1)^2\right)} \\ r = \left(\dfrac{9}{2}\mathbf{S} : \mathbf{S} : \mathbf{S}\right)^{1/3} = \left(\dfrac{27}{2}(\sigma_1 - \sigma_m)(\sigma_2 - \sigma_m)(\sigma_3 - \sigma_m)\right)^{1/3} \end{cases} \tag{5}$$

The variable $\sigma_1$, $\sigma_2$ and $\sigma_3$ in Eq. (5) represent the three principal stresses. $p$ and $\overline{\sigma}$ are the hydrostatic pressure and Von-Mises equivalent stress. $\mathbf{S}$ denotes the deviatoric stress tensor.

Figure 1(a) represents the Lode angle and deviatoric plane with the principal stresses. Figure 1(b) represents the stress-strain curve showing the three main stages (elastic stage, plastic stage, and damage evolution stage) before element failure at point $Q_3$. The plasticity model abovementioned corresponds to the second stage ($Q_1Q_2$).

As shown in Fig. 1(b), once the stress exceeds the initial yield strength at $Q_1$, the plastic deformation begins and accumulates in the deformed material until it reaches ultimate yield strength at $Q_2$. The critical plastic strain at that point is depicted by $\varepsilon_{\mathrm{d}}$, which is computed by the damage model [15] represented by the following equation:

$$\varepsilon_d = \left\{ \begin{array}{l} \left[\dfrac{1}{2}\left(D_1\exp(-D_2\eta) + D_5\exp(-D_6\eta)\right) - D_3\exp(-D_4\eta)\right]\overline{\theta}^2 + \\ \left[\dfrac{1}{2}\left(D_1\exp(-D_2\eta) + D_5\exp(-D_6\eta)\right)\right]\overline{\theta} + D_3\exp(-D_4\eta) \end{array} \right\} \\ \times\left(1 + D_7\mathrm{In}\left(\dfrac{\dot{\varepsilon}_p}{\dot{\varepsilon}_0}\right)\right)\left(1 + D_8\left(\dfrac{T - T_0}{T_m - T_0}\right)\right) \tag{6}$$

The parameters $D_1$~$D_8$ in Eq. (6) are the damage model coefficients [25]. Once the damage initiates, the stresses in the material can no longer increase but decrease drastically, which is the damage evolution stage ($Q_2Q_3$) as it showed in Fig. 1(b). Amongst four damage evolution modes available in the FEA package [10], the one involving fracture energy criterion and exponential degradation function is employed in this research work as given by Eq. (7):

$$D = 1 - \exp\left(-\int_{\varepsilon_d}^{\varepsilon} \overline{\sigma}L / G_f d\varepsilon\right) \tag{7}$$

where $D$ is the degradation parameter. The parameters $L_c$ and $G_{\mathrm{f}}$ are the characteristic length of the element and fracture energy, respectively. $L_c$ is derived by Eq. (8).

$$L_c = \begin{cases} \sqrt{l_1 \cdot l_2} & i = 4 \\ \sqrt[3]{l_1 \cdot l_2 \cdot l_3} & i = 6 \end{cases} \tag{8}$$

The parameters $l_1$, $l_2$ and $l_3$ are the length, height, and width of the element, respectively. $G_f$ is equal to 18.5 KJ/m$^2$ [26]. Table 1 summarizes the other constitutive model coefficients. All these parameters are input to Abaqus/Explicit using user defined subroutine VUMAT which is to be illustrated in next section.

Finally, the stress tensor $\sigma_i^r$ is updated with the degradation parameter as shown by Eq. (9),

$$\sigma_i^r = (1 - D)\sigma_i^t \tag{9}$$

where $\sigma_i^r$ and $\sigma_i^t$ stand for the stress with and without stiffness degradation, respectively. The superscript '$r$' means 'real or true stress' and '$t$' means 'trial stress'. The subscript $i$ in Eq. (9) is the number of stress components, which is 4 for 2-D and 6 for 3-D. It should be noted that the degradation parameter $D$ can never reach one when using exponential formulation in Eq. (7), so the point $Q_3$ in Fig. 1(b) does not locate exactly on the horizontal axial. Therefore, the degradation criterion is set as 0.99 in default under such condition [10].

**Table 1**
Coefficients of the constitutive model [15,26].

| Plasticity model | | Damage initiation model |
|---|---|---|
| $A$ = 812 MPa | $T_m$ = 1620 °C | $d_1$ = 0.694 |
| $m$ = 625.7 MPa | $h$ = 1 | $d_2$ = 0608 |
| $n$ = 0.176 | $\eta_0$ = −1/3 | $d_3$ = 0.263 |
| $B$ = 0.4 | $c_\eta$ = 0.212 | $d_4$ = 0.734 |
| $C$ = 0.073 | $c_\theta^s$ = 0.795 | $d_5$ = 0.43 |
| $E$ = 3939 | $c_\theta^t$ = 1.061 | $d_6$ = 0.04 |
| $\dot{\varepsilon}_0$ = 0.05 s$^{-1}$ | $c_\theta^c$ = 1 | $d_7$ = −0.028 |
| $T_r$ = 20 °C | $a$ = 4 | $d_8$ = 3.87 |

### 2.2. Constitutive model implementation in Abaqus FEA software using VUMAT subroutine

Since the previous constitutive model is not available in Abaqus FEA software, a VUMAT subroutine was developed to implement this model is this software. The flowchart of this subroutine is shown in Fig. 2.

It can be noticed that the properties of the work material including the coefficients of the constitutive model are read from the user defined material database in Abaqus Explicit CAE [10]. The thermal-mechanical properties for both workpiece and tool are given in Table 2.

The subroutine starts with the Lamé's constants, which are calculated using the Poisson's ratio and Young's modulus of the work material with Eq. (10).

$$\begin{cases} \mu = \dfrac{E_Y}{2(1+\nu)} \\ \lambda = \dfrac{2\mu(E_Y - 2\mu)}{(6\mu - 2E_Y)} \end{cases} \tag{10}$$

These two constants will be used to establish the elastic stiffness matrix. Then, the trial stresses can be calculated using the stiffness matrix by assuming that it is in an elastic stage. Afterwards, the state of element is estimated by comparing the calculated equivalent stress with the yield strength obtained from last incremental step. If the equivalent stress is lower, the element is really in an elastic stage. Thus, the stress components inside the element are taken as the final stresses. Otherwise, these components should be updated using the developed plasticity model given in Eqs. (1)–(3). In this case, the plastic strain increment $\Delta\varepsilon$ and plastic strain rate $\dot{\varepsilon}$ are calculated by the following equation,

$$\begin{cases} \Delta\varepsilon_p^i = \left(\sigma_t^i - \sigma_y^i\right) \Big/ \left(3\mu + H_d^i\right) \\ \dot{\varepsilon}_p^i = \Delta\varepsilon_p^i \Big/ \Delta t^i \end{cases} \tag{11}$$

where $\Delta_t^i$ is the step time increment. $H_d^i$ is the hardening coefficient that is the derivative of modified plasticity model with respect to the plastic strain. As given in Eq. (12), it will be updated as $H_d^{i+1}$ for next time increment once $\Delta\varepsilon$, $\dot{\varepsilon}_0$, stress triaxiality, Lode angle

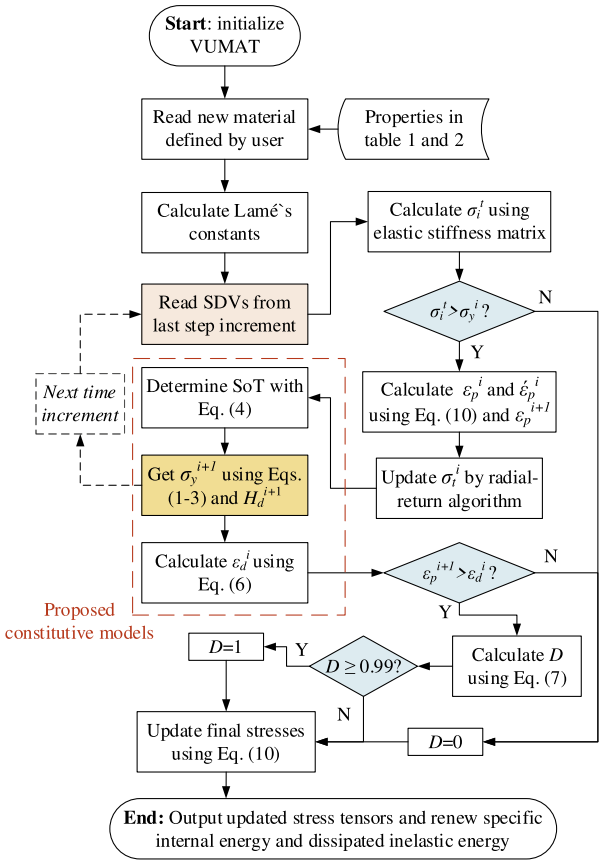


**Fig. 2.** Flow chart of VUMAT subroutine (SDVs: state dependent variables).

**Table 2**
Thermal and mechanical properties of workpiece and tool materials [26].

| Property | Unity | Ti6Al4V | WC—Co |
|---|---|---|---|
| Density, $\rho$ | Kg/m$^3$ | 4430 | 11,900 |
| Young's modulus, $E_Y$ | GPa | 109 | 534 |
| Poisson's ratio, $\nu$ | – | 0.34 | 0.22 |
| Specific heat capacity | J/(Kg K) | 611 | 400 |
| Thermal conductivity | W/(m K) | 6.8 | 50 |
| Coef. thermal expansion | K$^{-1}$ | $10^{-5}$ | – |

parameter, and the new plastic strain $\varepsilon_p^{i+1}$ are all determined.

$$H_d^{i+1} = \left(\left(mn\left(\varepsilon_p^{i+1}\right)^{n-1}\right)\left(B + CIn\left(E + \frac{\dot{\varepsilon}^{i+1}}{\dot{\varepsilon}_0}\right) + \left(\frac{C}{\Delta\varepsilon_p^i + \Delta t^i E\dot{\varepsilon}_0}\right)\left(A + m\left(\varepsilon_p^{i+1}\right)^n\right)\right)\right) \times \left(1 - \left(\frac{T^i - T_0}{T_m - T_0}\right)^h\right) \times \left(1 - c_\eta\left(\eta^{i+1} - \eta_0\right)\right)\left(c_\theta^s + \left(c_\theta^{ax} - c_\theta^s\right)\left(\gamma^{i+1} - \frac{\gamma^{a+1}}{a+1}\right)\right) \tag{12}$$

It should be noted in Eq. (12) that the derivative of the strain rate term is an approximation by neglecting the difference of $\Delta\varepsilon_p$ and $\Delta t$ between two adjacent time increments. In the meanwhile, the yield strength is updated as $\sigma_y^{i+1}$ through Eqs. (1)–(3). These two values will be saved as SDV (Sate Dependent Variables) and called in the next time increment in the same way. After this, $\varepsilon_d$ is updated to estimate if the element evolved to the damage stage. If so, the degradation value $D$ is calculated. For model with LAG-SL and LAG-nSL, the element is deleted if $D$ reaches 0.99. In the case of CEL, the element with complete degradation still flows inside the Eulerian part.

## 3. Orthogonal cutting models

### 3.1. Cutting models based on the LAG formulation (LAG-SL and LAG-nSL)

Orthogonal cutting models for titanium alloy are developed based on the LAG formulation, with and without sacrificial layer, hereby named by LAG-SL and LAG-nSL, respectively. These two models are shown in Fig. 3.

The geometry of the workpiece is 2 mm in length and 0.5 mm height, while of the tool is 0.3 mm in width and 0.5 mm height. As

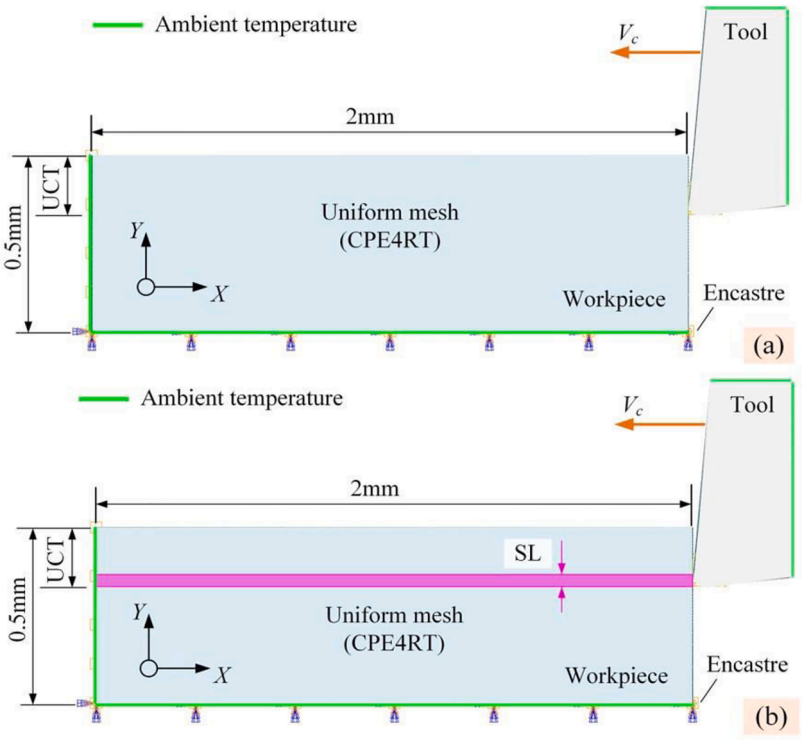


**Fig. 3.** Orthogonal cutting models using LAG formulation: (a) LAG-nSL and (b) LAG-SL.

seen in Fig. 3(a) and (b), the only difference between LAG-SL and LAG-nSL models is the sacrificial layer (SL), which is located just in front of the tool cutting edge. The thickness of the SL is assumed equal to the cutting edge radius, which is frequently used to facilitate the material separation from the workpiece to form the chip [21,27]. The element type for both models is selected as 4-node bilinear displacement and temperature, reduced integration with hourglass control (CPE4RT). Noted that a uniform mesh with quadratic element geometry of 7.1 μm × 7.1 μm is assigned for the whole workpiece (including the SL). The reason for this geometry is to have equivalent characteristic length between 2D LAG-based models and 3D CEL-based model (described in the next section). As seen, the tool is moving in the cutting direction (*X*-direction) at a constant velocity (the cutting speed) and its movement is constrained in the *Y*-direction, while the workpiece is movement is constrained in both *X* and *Y* directions at its bottom surface.

The constitutive model (both plasticity and damage parts), and the thermal and elastic properties of the work material are given in the previous sections. It is worth to point out that the damage model was applied to whole the workpiece in the case of the LAG-nSL model, and only to the uncut chip layer and sacrificial layer in the case of the LAG-SL.

The interface heat transfer coefficient between the tool and workpiece/chip is 1000 KW/($m^2$-K) [28]. Heat convection and heat radiation phenomena between the external surfaces of the workpiece/chip/tool and the environment was not considered. The main reason is to have identical thermal boundary conditions in both LAG-based and CEL models, because it is not possible to apply convective/radiative heat exchanges between the external surfaces of the workpiece/chip/tool and the environment in the case of the CEL model.

It is worth noting that an error of excessive element distortion will arise for the LAG-nSL and LAG-SL models when using a self-contact only applied to the external surfaces (hereby called external self-contact) of the workpiece (for LAG-nSL model) or the uncut chip layer (for LAG-SL model). To solve this problem, an additional self-contact is also applied to all the elements of the workpiece (hereby called internal self-contact). Therefore, the distorted element will be in normal contact with the neighbor elements, instead of being severely stretched or penetrating other elements, which thereby causes the distortion error.

Regarding the contact conditions at the tool-chip and tool-workpiece interfaces, the contact model proposed by Zorev [30] considering both plastic and elastic (sliding) regions is adopted as shown by the following equation:

$$\tau_f = \begin{cases} \sigma_y \Big/ \sqrt{3}, & \text{if} \quad \mu\sigma_N > \sigma_y \Big/ \sqrt{3} \\ \mu_f \sigma_N & \mu\sigma_N \le \sigma_y \Big/ \sqrt{3} \end{cases} \tag{13}$$

In Eq. (13), $\sigma_y$ and $\sigma_N$ stand for the yield stress of chip material and the normal stress at the chip-tool interface, respectively. The parameter $\mu_f$ represents the friction coefficient which is dependent on the contact conditions, including the sliding velocity, and it is represented by the following equation [31]:

$$\mu_f = 0.48 \cdot V_s^{-0.194} \tag{14}$$

This contact model is used in the three cutting models presented in Fig. 4).

### 3.2. *Cutting model using CEL formulation*

Compared with the LAG-based models in Fig. 3, CEL-based model depicted in Fig. 4 shows several differences.

It can be noticed from Fig. 4 that the workpiece is included in a Eulerian region with a parallelogram shape, instead of rectangular one used in LAG-based models. This is because CEL was found very sensitive to the mesh orientation and improper definition can lead to invalid results like extremely high strains [15]. After performing several simulations using different orientation angles, an angle equal to the tool rake angle was determined to show the most reasonable results. Besides the mesh orientation, the width of the CEL

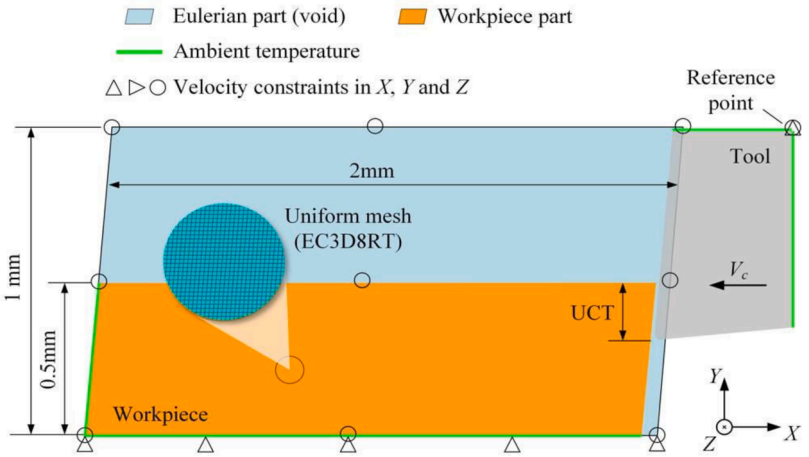


**Fig. 4.** Orthogonal cutting model using CEL formulation.

model (not represented in Fig. 4) is required, which is equal to 0.01 mm. As for the meshing, an 8-node thermally coupled linear Eulerian brick with reduced integration and hourglass control (EC3D8RT) is applied to the whole Eulerian region. The workpiece is obtained through partition and material assignment inside the Eulerian region. Besides, a uniformly refined mesh with a geometry of 6 μm × 6 μm is assigned to the Eulerian region, which was determined based on the work of Xu et al. [15]. It is worth mentioning that the Eulerian element is three-dimensional while those Lagrangian used in the LAG-based models are two-dimensional. Therefore, to ensure the equivalence between the three models, the characteristic length should be the same [24]. According to Abaqus user manual [10], the characteristic length for two-dimensional element is the square root of its area, and that for three-dimensional one is the cubic root of its volume. Thus, a mesh of 7.1 μm × 7.1 μm is applied for LAG-SL and LAG-nSL correspondingly. As for the tool, it follows the Lagrangian formulation with an element type of 8-node thermally coupled linear brick, trilinear displacement with reduced integration and hourglass control (C3D8RT). At the bottom boundary of the workpiece part, the velocity in both *X* and *Y* directions are set as zero. To ensure that the cutting process is under plane strain conditions, another constraint with zero velocity in *Z* direction is designated to the front and back sides of the Eulerian part. The thermal boundary conditions and the contact model are the same as those used in LAG-based models.

### *3.3. Models for simulating the cooling process to obtain the residual stresses*

To calculate the RS induced by machining, the workpiece should be unloaded and cooled down to room temperature, as described by Outeiro [38]. Since the workpiece unloading was already simulated with the previous cutting models, only the cooling phase needs to be simulated to obtain the RS. This cooling phase was simulated differently in LAG-based and CEL models.

In the case of the LAG-based models, before simulate the cooling process the workpiece and the corresponding data is transferred from Abaqus/Explicit (explicit time integration) to Abaqus/Standard (implicit time integration). Figure 5 shows a schematic representation of the model of the cooling process in Abaqus/Standard with the corresponding boundary conditions. To simulate the cooling process, a room temperature boundary condition is added to the left and bottom surfaces of the workpiece, and a heat convection (referred as surface film condition in Abaqus) was applied to the surfaces exposed to air. A heat convection coefficient of 23 W/(m$^2$-K) is applied [29].

In the case of the CEL model, the simulation of the cooling process is performed still in Abaqus/Explicit, due to the complexity to transfer the data from Abaqus/Explicit to Abaqus/Standard, which involves data transfer from EC3D8RT Eulerian element used in Abaqus/Explicit to CPE4RT element used in Abaqus/Explicit. Only a room temperature boundary condition is added to the left and bottom surfaces of workpiece.

After these calculations, the RS were extracted from the models by applying the procedure described by Outeiro [38].

## 4. Orthogonal cutting tests and post-process characterizations

To evaluate the accuracy of each formulation to simulate the orthogonal cutting process of Ti6Al4V alloy, the predicted results in terms of chip morphology, forces, and RS were compared with those results obtained by Cheng et al. [32], who performed a series of orthogonal cutting tests in planning configuration using the same work material. A description of the experimental setup and cutting conditions used by Cheng et al. [32] is described as follows.

### *4.1. Conditions of orthogonal cutting tests*

The cutting tool material was uncoated WC—Co carbide. The information of the seven cutting tests can be found in Table 3 where the parameters $h$ and $r_n$ represent the UCT and tool cutting edge radius, respectively. The tool rake angle is denoted by $\gamma_n$ and the flank angle by $\alpha_n$.

Prior to the tests, the edges of all the cutting tools were measured with 3D optical profilometer (Alicona, Infinite Focus SL). By means of a custom fixture, the workpiece specimen is connected to a piezoelectric dynamometer (Kistler, 9119AA2), which permitted

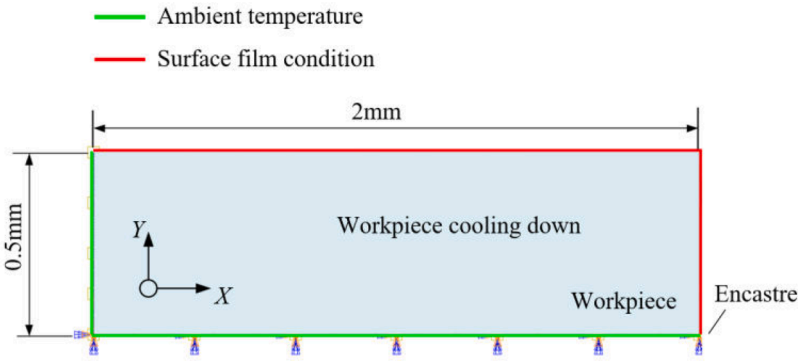


**Fig. 5.** Simulation of the cooling process for RS calculation with LAG-based models.

**Table 3**
Cutting conditions adopted in orthogonal cutting tests and numerical simulations.

| Cutting condition No. | $h$ (mm) | $r_n$ (μm) | $V_c$ (m/min) | $\gamma_n$ (deg) | $\alpha_n$ (deg) |
|---|---|---|---|---|---|
| 1 | 0.15 | 16 | 60 | −6 | 6 |
| 2 | 0.15 | 30 | 60 | −6 | 6 |
| 3 | 0.15 | 16 | 20 | 5 | 6 |
| 4 | 0.2 | 16 | 20 | 5 | 6 |
| 5 | 0.15 | 16 | 60 | 5 | 6 |
| 6 | 0.15 | 30 | 60 | 5 | 6 |
| 7 | 0.2 | 16 | 60 | 5 | 6 |

to measure the cutting (in the cutting direction) and thrust forces.

### 4.2. Post-process characterizations

Post-process characterizations are carried out in terms of the measurements of chip morphologies and residual stresses (RS). The chips were collected and then made as samples by mounting them in resins according to the ASTM standards [33]. Afterwards, the samples are observed under an optical microscope where the chip morphologies are recorded. For each cutting condition listed in Table 3, five measurements were performed.

Figure 7 shows one of the measurements of the chip peak thickness $d_{pk}$ and the pitch distance $d_{ph}$. With these two parameters, the maximum chip compression ratio ($CCR_m$) and the chip segmentation frequency ($f_{seg}$) can be calculated by the following expressions.

$$CCR_m = \frac{d_{pk}}{h} \tag{15}$$

$$f_{seg} = \frac{V_{ch}}{d_{ph}} = \frac{V_c}{CCR_m \cdot d_{ph}} \tag{16}$$

where $V_{ch}$ stands for the chip flow velocity. RS is measured on the machined workpiece as schematically represented in Fig. 8.

As illustrated in Fig. 8(a), the RS in both longitudinal direction and transversal direction are measured by means of X-ray diffraction technique using Seifert XRD 3000 PTS equipment. The X-ray diffraction conditions were presented in the work of Cheng and Outeiro [20]. An average value is adopted from the measurements in a rectangular region (4 mm × 2 mm) at the center of the machined surface. Since the penetration depth of X-ray is about 5 μm, the distribution of RS beneath the machined surface are obtained by removing successive layers of material from the surface by electro-polishing. As seen in Fig. 8(b), in-depth RS profile can be characterized by four parameters [34–36], namely the maximum compressive residual stress (MRS) beneath the surface, the residual stress at the machined surface (SRS), the depth of MRS (DMRS), and the thickness of the layer affected by the RS (TLRS). Additionally, the root mean square error (RMSE) between the simulated and measured RS profiles is also used. This parameter permits to estimate the RS difference along the entire in-depth profile.

## 5. Results and discussion

### 5.1. Chip morphology

The chip morphology is acquired when the simulation of cutting process is stable. As shown in Figs. 5, 21 chip morphologies are obtained by performing the simulations for the 7 cutting conditions listed in Table 3, using the three cutting models.

As seen in Fig. 9, an apparent difference in all the simulated chip serrations can be noticed between the CEL formulation and the LAG-based ones. Using the CEL model, the chips are serrated but the chip segments are still connected. On the contrary, the chip

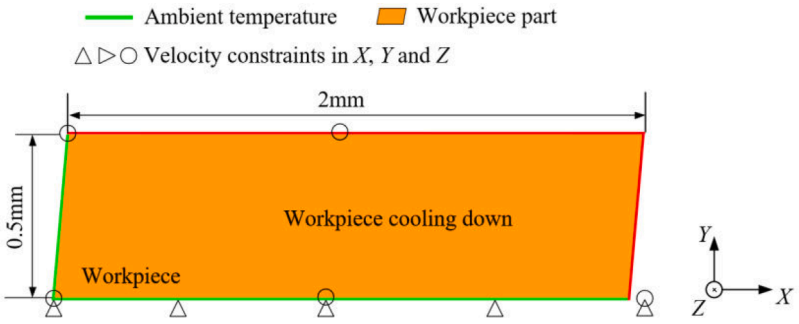


**Fig. 6.** Simulation of the cooling process for RS calculation with CEL model.

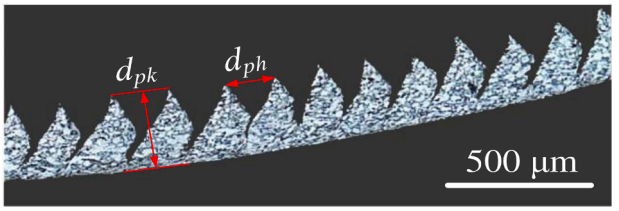


**Fig. 7.** The measurement on the chip morphology.

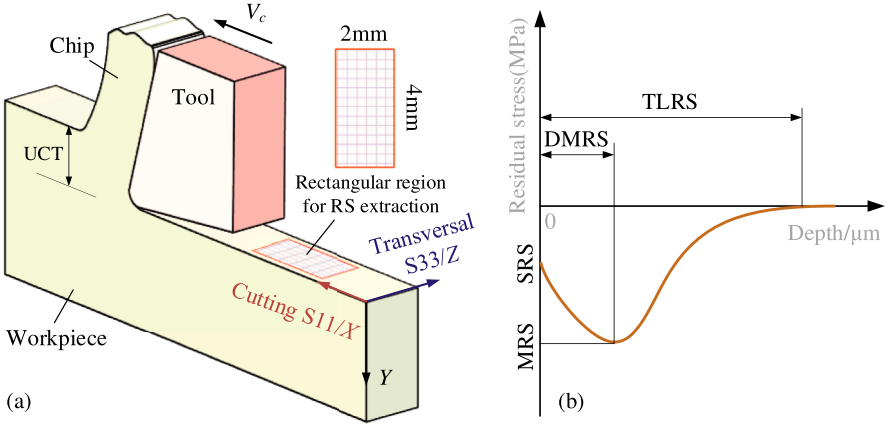


**Fig. 8.** Schematic representation of (a) the orthogonal cutting process showing the area where the RS were measured, and (b) a typical in-depth RS profile.

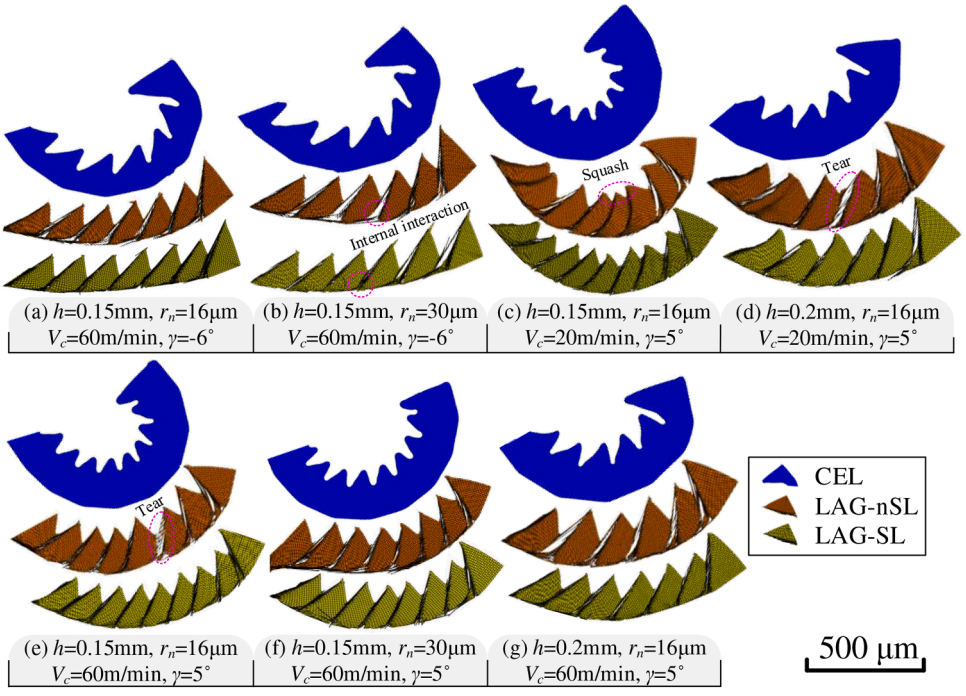


**Fig. 9.** Comparison of the chip morphologies simulated for the 7 cutting conditions listed in Table 3, using the 3 cutting models.

segments are not fully connected but slightly separated when using LAG-SL and LAG-nSL cutting models. This can be attributed to the element deletion technique and the internal self-contact that are used in the LAG-based models. These are however not available in CEL where the failed elements exist with zero stiffness, instead of being deleted. As far as LAG-SL and LAG-nSL models are concerned, the chip morphologies are very similar since the SL is the only difference between them. Nevertheless, a small difference can still be noticed among the distances between some adjacent segmentations. For an instance in Fig. 9(b), some visible "cracks" are generated using LAG-nSL model due to the internal self-contact. At corresponding positions in LAG-SL model, the "crack" is almost invisible. Such difference could also be found for other cutting conditions, especially in Fig. 9(d, f, g).

To quantify the differences among the simulated chip morphologies using the three cutting models, Fig. 10 shows the $CCR_{\mathrm{m}}$ and the $f_{\mathrm{seg}}$, calculated using Eqs. (15) and (16), respectively.

In the case of the $CCR_m$ in Fig. 10(a), it is noticed that the experimental measurements are underestimated by all the simulations where the smallest average error (9.5%) is yielded by LAG-nSL, followed by LAG-SL (16.9%) and CEL (20.3%). As for LAG-based formulations, such underestimation could be a result of the damage model which is assigned to the whole workpiece. Therefore, more elements are damaged and then deleted, which is far from the reality. As for CEL formulation, the underestimation may be because some elements near tool edge are compressed into machined surface since the elements have zero stiffness when they damaged. The comparisons in Fig. 10(a) evidenced that LAG-nSL can better predict $CCR_m$ compared to other models. Compared with the simulations under positive-rake-angle conditions ($\gamma = 5^{\circ}$ in No. 3–7), an even smaller error (3%) is found under negative-rake-angle cutting conditions ($\gamma = -6^{\circ}$ in No. 1–2). As far as the cutting edge radius is concerned, its increase from 16 to 30 μm (from No. 1 to 2, 5 to 6) induces little difference in $CCR_m$. As for the influence of the cutting speed, a slight increase is observed in the $CCR_m$ when the cutting speed increases from 20 to 60 m/min (from No. 3 to 5). On the contrary, $CCR_m$ is reduced when UCT increases from 0.15 to 0.2 mm (from No. 3 to 4, 5 to 7).

As far as $f_{\mathrm{seg}}$ is concerned, Fig. 10(b) reveals that LAG-nSL gives an average error of 48.5.6%, similar to the LAG-SL (49.9%) and CEL as the worst (137.7%). The increase of cutting edge radius from 16 to 30 μm (from No. 1 to 2, 5 to 6) leads to reduced $f_{\mathrm{seg}}$. With regards to cutting speed, its increase from 20 to 60 m/min (from No. 3 to 5) causes a significant increase of $f_{\mathrm{seg}}$. When UCT increases from 0.15 to 0.2 mm (from No. 3 to 4, 5 to 7), $f_{\mathrm{seg}}$ slightly decreased. From the comparisons and analysis above, it is concluded that LAG-nSL can better predict both $CCR_{\mathrm{m}}$ and $f_{\mathrm{seg}}$ than the other two cutting models.

### 5.2. *Cutting and thrust forces*

As a result of the cyclic nature of the cutting process, chip segmentation is occurring, and the forces are varying cyclically. Therefore, to compare the simulated forces with the experimental ones, the average values are calculated. Figure 11 shows both cutting, $F_c$, and thrust forces, $F_t$.

Figure 11(a) shows that for all cutting conditions the cutting forces $F_{\mathrm{c}}$ predicted using LAG-nSL model are higher than those predicted using other models, and they are closer to the experimental measurements. The average differences between predicted and measured $F_{\mathrm{c}}$ are 12.8%, 30.8%, and 32.5%, for LAG-nSL, LAG-SL, and CEL, respectively. Concerning the influence of the cutting conditions on $F_{\mathrm{c}}$, it is found from the experimental measurements that $F_c$ increases about 100N when the cutting edge radius increase from 16 to 30 μm (from cutting conditions 1 to 2, and from 5 to 6). Such increase is well predicted by the three models in conditions 5 to 6. This could be related to the huge error (±200N) in the measured $F_c$ in condition 2 which shows that there would have been slight change of $F_c$ in cutting condition 1 to 2. $F_{\mathrm{c}}$ also increases about 50N when the UCT increases from 0.15 to 0.2 mm (from cutting conditions 3 to 4, and from 5 to 7). Such increase is well predicted by the three models. A decrease of around 100N is observed from

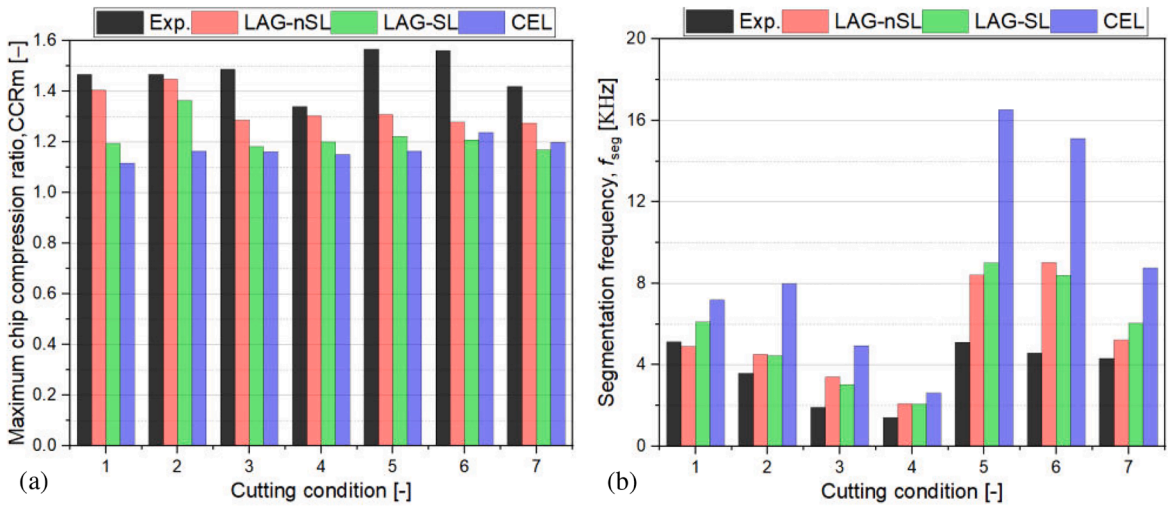


**Fig. 10.** Comparisons of (a) $CCR_{\mathrm{m}}$ and (b) $f_{\mathrm{seg}}$ between simulated and measured chips.

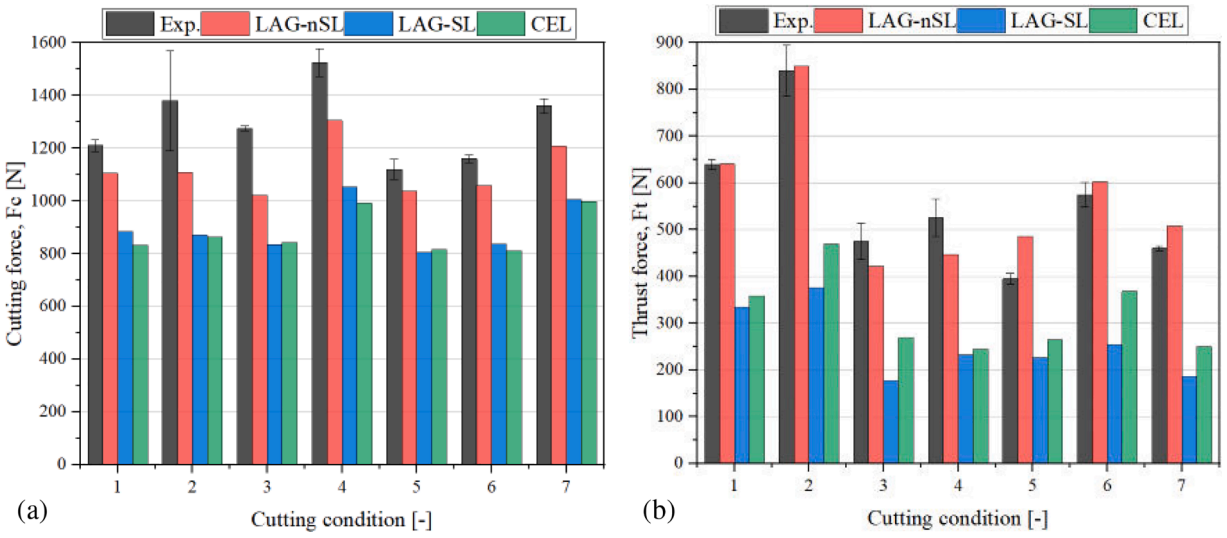


**Fig. 11.** Comparison between simulated and measured (a) cutting and (b) thrust forces.

experimental measurements when the cutting speed increases from 20 to 60 m/min (from cutting conditions 3 to 5). However, this decrease is not shown by any of the three models.

The differences between predicted and measured forces are more evident in the thrust direction. As illustrated in Fig. 11(b), significant deviations have been found between the experimental and simulated thrust forces, $F_t$, using LAG-SL and CEL models, involving an average error of 53.2% and 42.3%, respectively. Similarly high error up to 53% was also reported by Cheng and Outeiro [20] who developed a LAG-SL model to simulate machining of Ti6Al4V alloy. On the contrary, LAG-nSL exhibits excellent predictions with an average error of 9.3%. As aforementioned, such significant difference is attributed to the deformation near cutting edge since it contributes mostly the thrust force [2]. Additionally, the experimental measurements show that $F_t$ increases about 200N with the increase of cutting edge radius from 16 to 30 μm (from cutting condition 1 to 2, and from 5 to 6). The simulated results from LAG-nSL and CEL show similar increase while little change is noticed in those from LAG-SL. This can be explained by the existence of SL which weakens the effects of tool cutting edge microgeometry. An increase of around 50N is observed when the UCT increases from 0.15 to 0.2 mm (from cutting condition 3 to 4, and from 5 to 7). A similar increase is noticed in the results using LAG-nSL cutting model. However, the results from CEL show a contrary change while those from LAG-SL show an increase in cutting condition 3 to 4 but a decrease in 5 to 7. A decrease of around 100N is observed when the cutting speed increases from 20 to 60 m/min (from cutting condition 3 to 5). However, the simulations using LAG-nSL show an increase about 25N while CEL shows slight increase and LAG-SL shows little change. To sum up, among the three formulations, LAG-nSL gives the most satisfying predictions of both cutting force and thrust forces.

### 5.3. *Residual stresses*

The simulated RS in the cutting (S11) and transversal(S33) directions and the corresponding experimental values from Cheng et al. [20] are given in Figs. 12 and 13, respectively.

As seen from the experimental results shown in Fig. 12, the RS in the cutting direction (S11) is highly compressive at surface (around −300 ~ −500 MPa) and increases to a maximum value in compression (MRS) below the surface, located at a depth near 30–50 μm depending on the cutting conditions. Afterwards, the RS decreases in compression until reach 0 MPa at a depth around 100–150 μm depending on the cutting conditions. An exception is observed in Fig. 12(f), where the experimental in-depth RS profiles do not show a MRS below the surface. In this case, the RS is maximal at surface, decreasing progressively in compression as the depth below surface increases, until reaching 0 MPa at a depth of about 135 μm. Similar in-depth RS profile is found from the perspective of the simulations. It is noticed that RS simulated by both LAG-SL and LAG-nSL end in tensile state (30–150 MPa), instead of stabilizing at 0 MPa. Nieslonly et al. [37] also observed such behavior of the in-depth RS profile in their LAG-based simulations. This might be attributed to the stress equilibrium inside the workpiece. On the contrary, a slight compressive state (−50~−80 MPa) is found at the end of the in-depth RS profile calculated using CEL. Such differences between simulated RS obtained using the three cutting models could due to two main reasons: 1) the numerical methods used to simulate the material separation to form the chip, and 2) to the procedure used to simulate the cooling process to calculate the RS. Concerning the first reason, since the RS formation is closely related to the thermomechanical phenomena induced by cutting, the accuracy of the RS prediction strongly depends on how accurate is the model to predict the forces and temperatures in cutting. As seen previously, the LAG-nSL model can accurately predict the forces, in particular the thrust force, while the other two cutting models largely underestimate these forces. Concerning the second reason, heat convection was only used to simulate the cooling process of the LAG-based models and not used in the CEL model.

As shown in Fig. 13, the results of RS in S33 direction reveal that the SRS are slight tensile or compressive (−50~+70 MPa), which

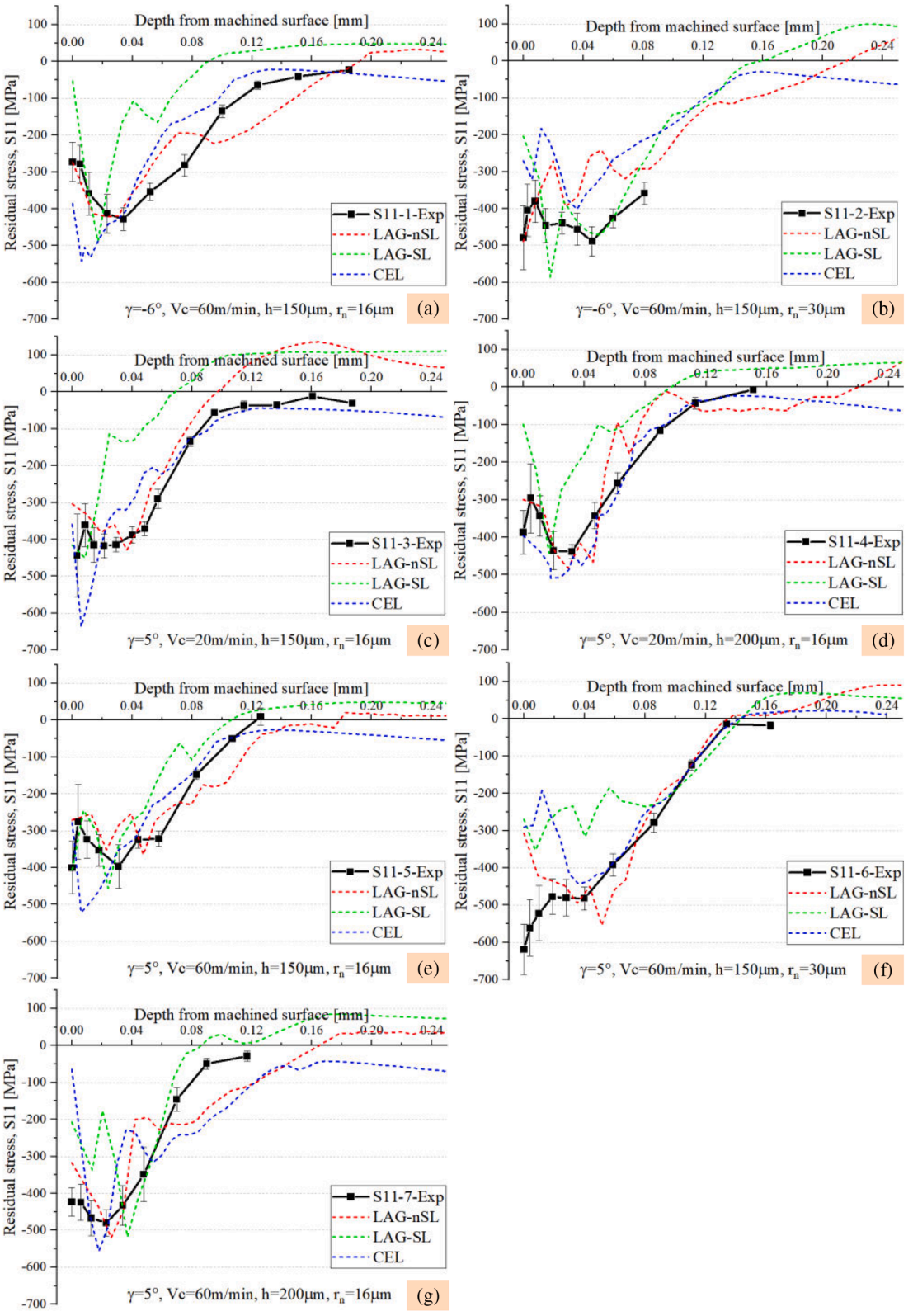


**Fig. 12.** Experimental and simulated RS in the cutting (S11) direction.

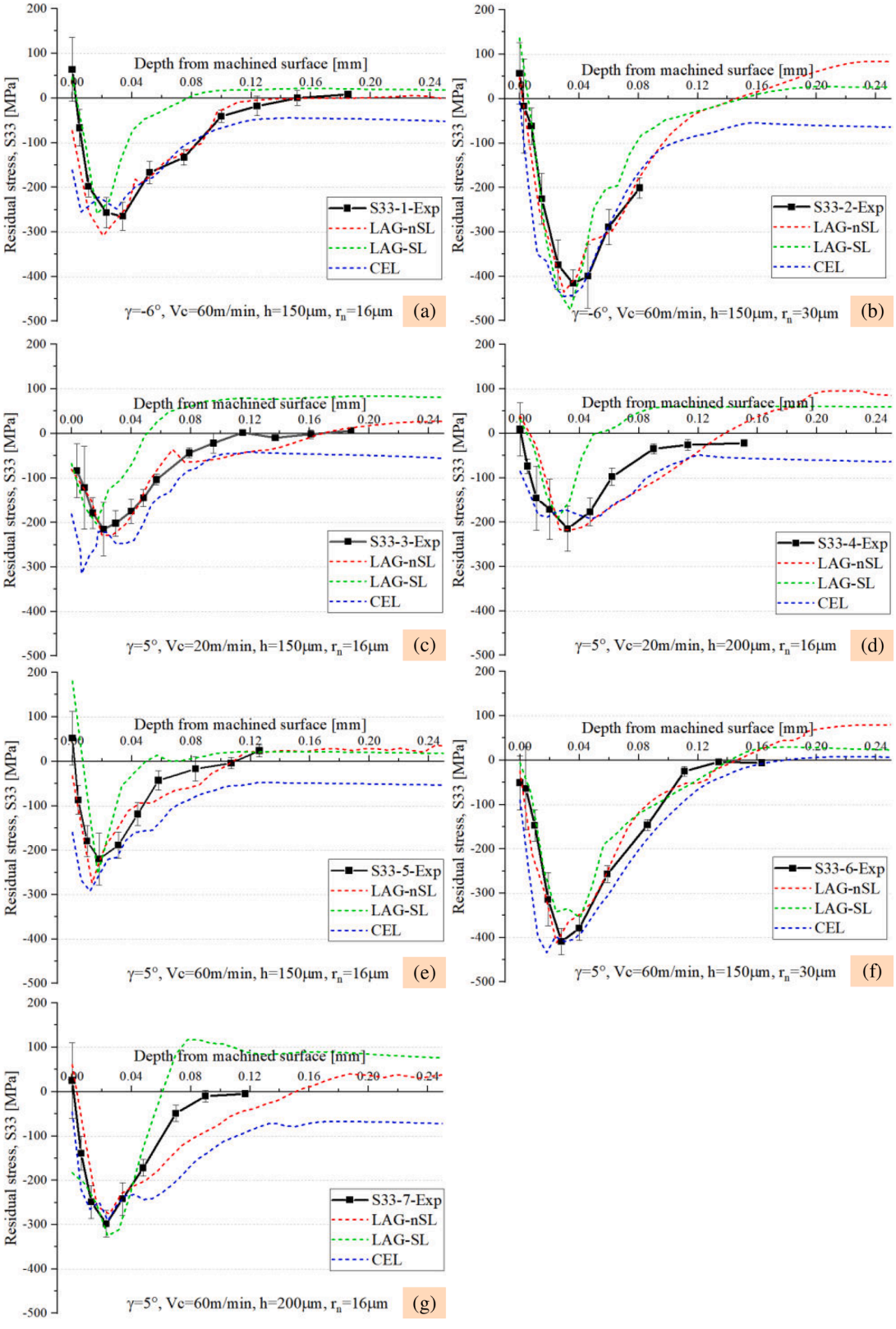


**Fig. 13.** Experimental and simulated RS in the transversal (S33) direction.

is different from the highly compressive SRS in S11 direction given in Fig. 12. Moreover, the MRS is less compressive (around −200∼−400 MPa) when compared with that in S11 (−400∼−500 MPa). It is also found that the RS profiles from LAG-based simulations still end tensile (0∼100 MPa) while those from CEL compressive (−100∼0 MPa) except in Fig. 13(f) where the RS ends slight tensile (0∼10 MPa). In addition to the reasons aforementioned, the boundary constraint in *Z* direction (see Fig. 8(a)) could also contribute to such difference. This has to be additionally controlled by zeroing the velocity in *Z* direction for CEL formulation. As far as the profiles along the depth machined surface to DMRS is concerned, a much better agreement can be observed between the measurements and all the simulations in S33 direction than those in S11.

To better analyze the differences between the experimental and simulated in-depth RS profiles in both cutting and transversal directions, the four parameters associated to this profile (see Fig. 6), namely SRS, MRS, DMRS, DAL and RMSE are discussed as follows.

Figures 14 and 15 show the results of surface residual stress in cutting direction (SRS-1) and transversal direction (SRS-2) obtained from the experiments and the three simulation models. The results in Fig. 14 indicate that LAG-nSL formulation gives better predictions in cutting condition No. 1, 2 and 7, LAG-SL in No. 3, and CEL in No. 4 and 5. Fig. 15 reveals that LAG-nSL shows higher prediction accuracy in cutting condition No. 2, 3, 5, 6 and 7, LAG-SL in No. 1, 3, and 4. It is more apparent regarding SRS-2 in Fig. 15. The reason for this could be the electric polishing procedure which removes certain microns of material from workpiece surface for the acquisition of IRS. Therefore, this could have a huge difference on the RS at topmost surface.

Figures 16 and 17 present the results of the maximum compressive residual stress in the cutting direction (MRS-1) and transversal direction (MRS-2) from the experiments and three simulation models. It is found that the model using CEL overestimates MRS-1 for cutting condition No. 1, 3, 4, 5 and 7, and MRS-2 for No. 2, 5 and 6. LAG-nSL suggests close predictions in condition No. 1–5 but overestimations in No. 6–7.

Figures 18 and 19 display the results of the depth of the maximum compressive residual stress in cutting direction (DMRS-1) and transversal direction (DMRS-2) from experiments and three simulation models. The comparisons signify that the model using CEL underestimates the DMRS-1 for all 7 cutting conditions and DMRS-1 for 1–6 conditions. On the contrary, the model using LAG-nSL tends to overestimate the DMRS, concerning its outcomes for condition No. 1, 3, 5, 6, 7 in Fig. 18 and No. 1, 2, 4, 6, 7 in Fig. 19. Figures 20 and 21 include the results of the depth of the residual stress affected layer in cutting direction (TLRS-1) and transversal direction (TLRS-2) from both experiments and the three simulation models. It should be noted that the profiles yielded from simulations do not end at 0 MPa as aforementioned. Therefore, for LAG-based simulations, the depth of the point where the profile intersects with 0 MPa axis is taken as the TLRS. As for CEL simulations, the depth of the point which is at the end part and closest to 0 MPa axis is treated as the DAL. In this way, it can be found from the comparisons that compared with experimental measurements, larger values of TLRS are obtained when using LAG-nSL in view of predicted TLRS-1 in cutting conditions No. 1, 4, 5 and 7 and TLRS-2 for No. 1, 3, 4, 6 and 7. On the contrary, smaller values of TLRS are yielded by LAG-SL regarding the results of both TLRS-1 and TLRS-2 in No. 1, 3, 4, 5, 7. Such difference could stem from the presence of SL.

Figures 22 and 23 show the results of the root mean square error of RS curve in cutting (RMSE-1) and transversal direction (RMSE-

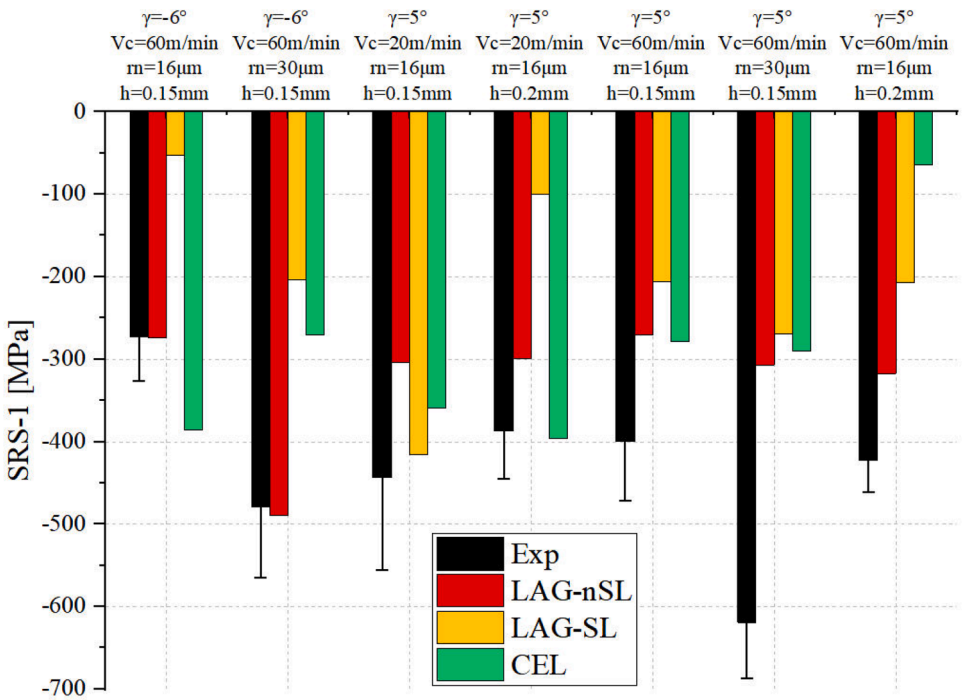


**Fig. 14.** Results of initial RS in cutting direction (SRS-1) from experiments and three simulation models.

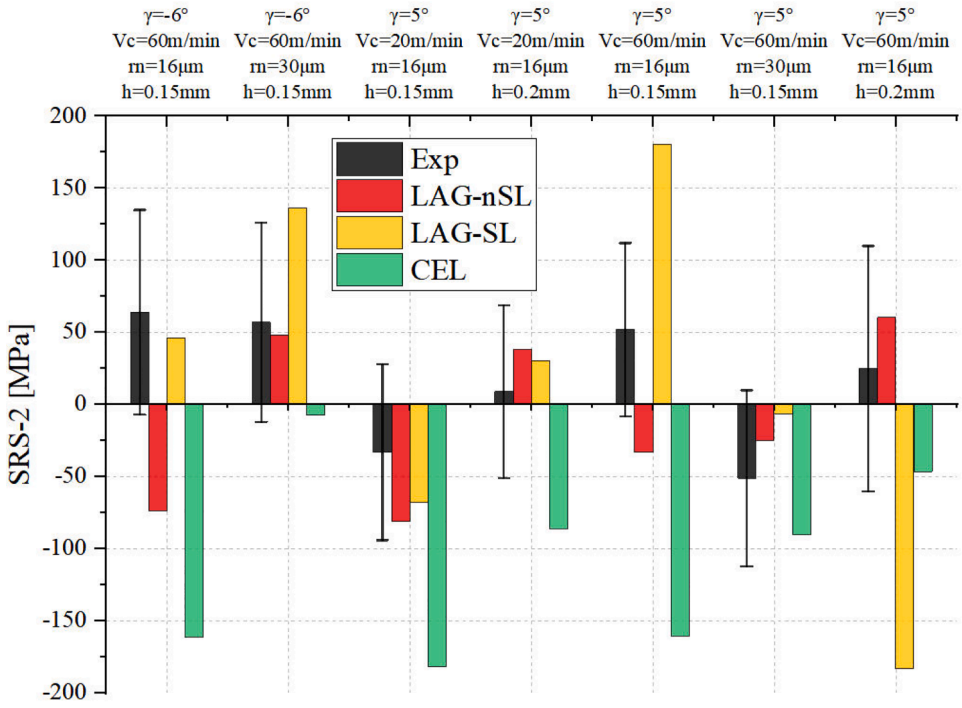


**Fig. 15.** Results of initial RS in transversal direction (SRS-2) from experiments and three simulation models.

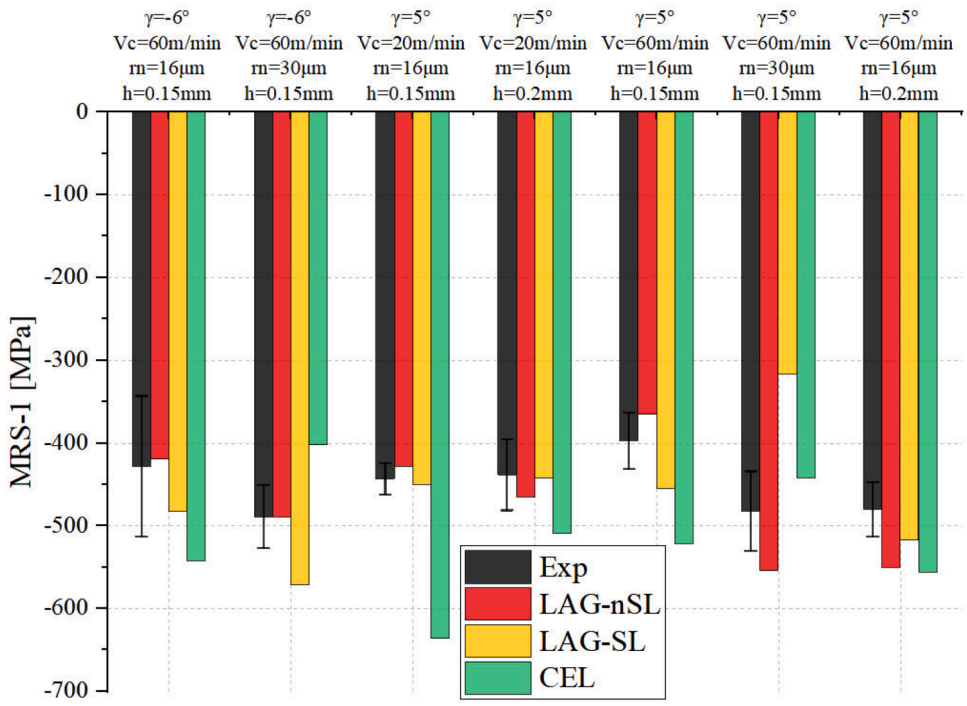


**Fig. 16.** Results of the maximum compressive RS in cutting direction (MRS-1) from experiments and three simulation models.

2), respectively. Taking 100 MPa as the admissible error in RMSE-1, one can find that LAG-nSL is qualified for all cutting conditions except No. 6. LAG-SL gives acceptable results in condition No. 5 and 7 while CEL in No. 4 and 5. As for RMSE-2, the admissible error is set as 50 MPa. Therefore, LAG-nSL gives reasonable predictions in condition No. 2, 3, 5, 6, 7 while LAG-SL in merely No. 6 and CEL in

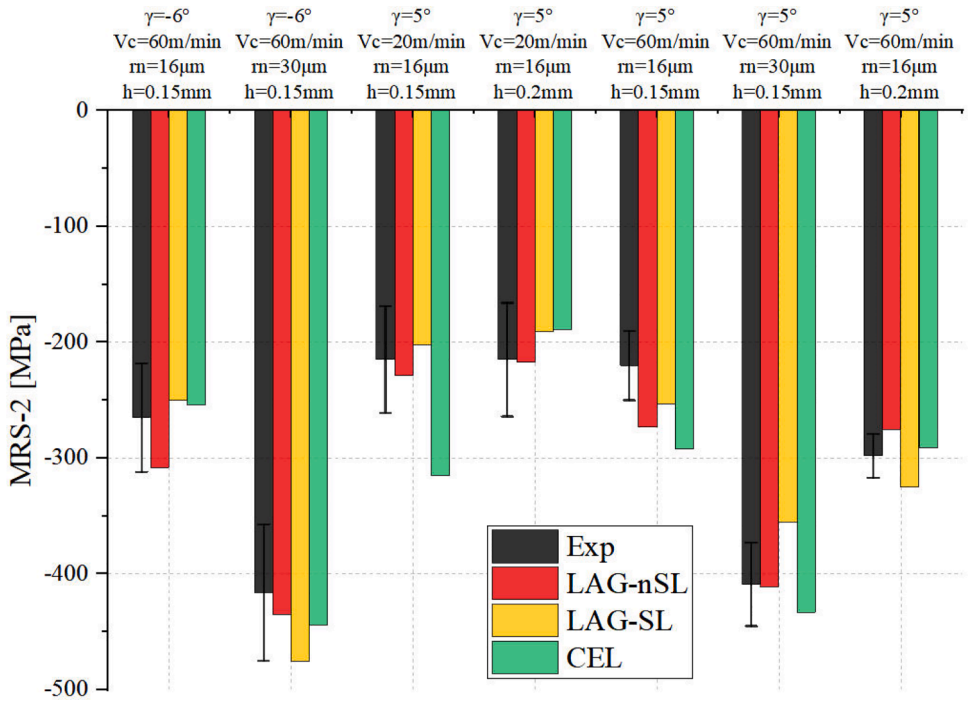


**Fig. 17.** Results of the maximum compressive RS in transversal direction (MRS-2) from experiments and three simulation models.

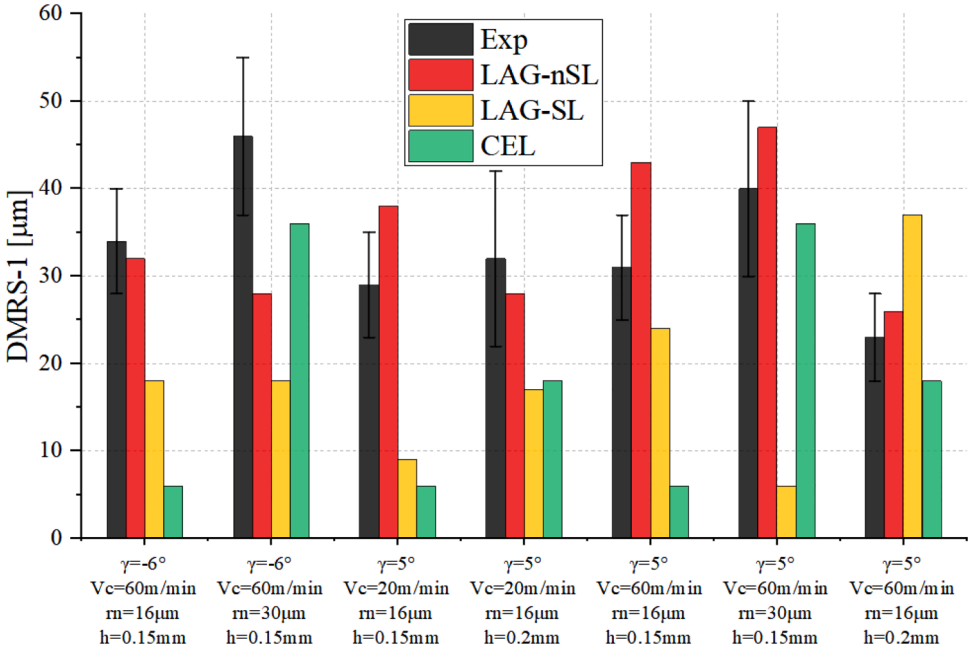


**Fig. 18.** Results of the depth of the maximum compressive RS in cutting direction (DMRS-1) from experiments and three simulation models.

No. 4.

From the results in Figs. 14–21 and the analysis above, an overall evaluation of the preference of the three formulations can be conducted with regards to the four parameters. By treating the 7 cutting conditions as 7 points, the formulation can acquire one point when the yielded results are within the errors of experimental measurements. Therefore, the final score for each formulation ranges from 1 to 7, according to which a preference ratio can be separately calculated as collected in Fig. 24.

As depicted in Fig. 24, the highest preference ratios are found when using LAG-nSL in calculating SRS (99% in total for two

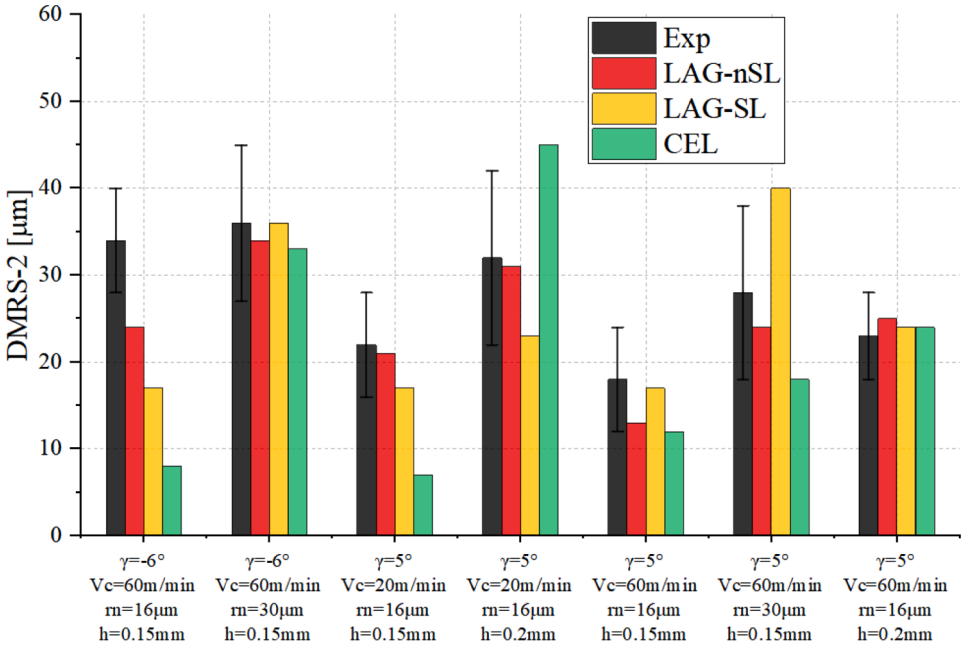


**Fig. 19.** Results of the depth of the maximum compressive RS in transversal direction (DMRS-2) from experiments and three simulation models.

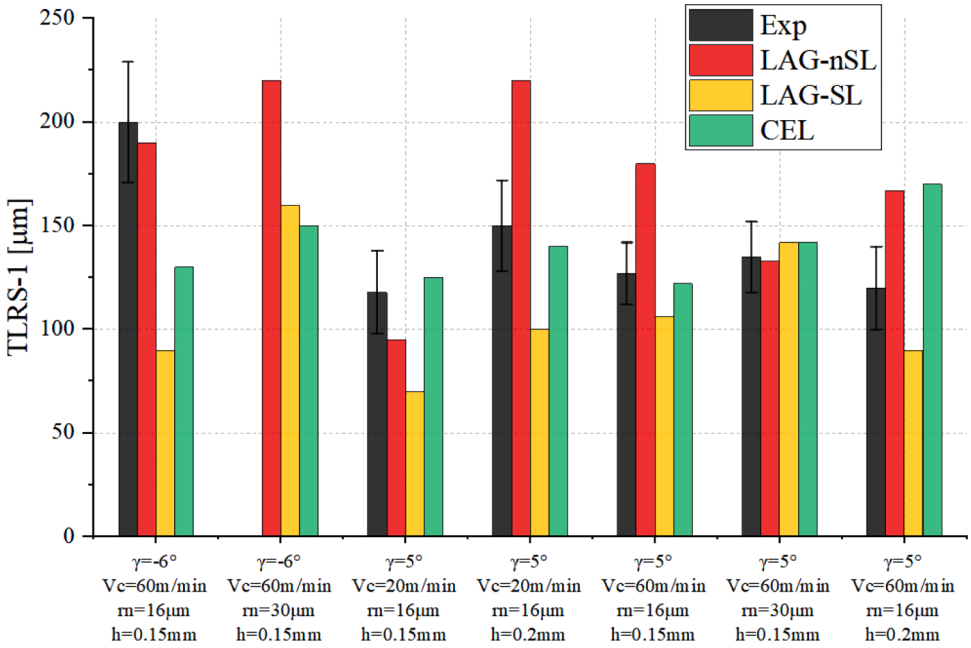


**Fig. 20.** Results of the depth of the RS affected layer in cutting direction (TLRS-1) from experiments and three simulation models.

directions), MRS (85%), DMRS (107%) and RMSE (128%). On the contrary, the cutting model using LAG-SL gains equally high preference ratio as LAG-nSL in MRS, but it shows very low preference ratio in SRS (47%), TLRS (26%) and RMSE (32%). Such a huge difference between LAG-nSL and LAG-SL reveals that the removing of SL is desired to characterize better the formation near machined surface and thereby more accurate RS distribution. CEL-based cutting model obtains the highest preference ratio in TLRS (100%) and the lowest ones in MRS (39%) and DMRS (44%). This signifies that CEL-based model predicts better the RS distribution after TLRS but worse the one near machined surface.

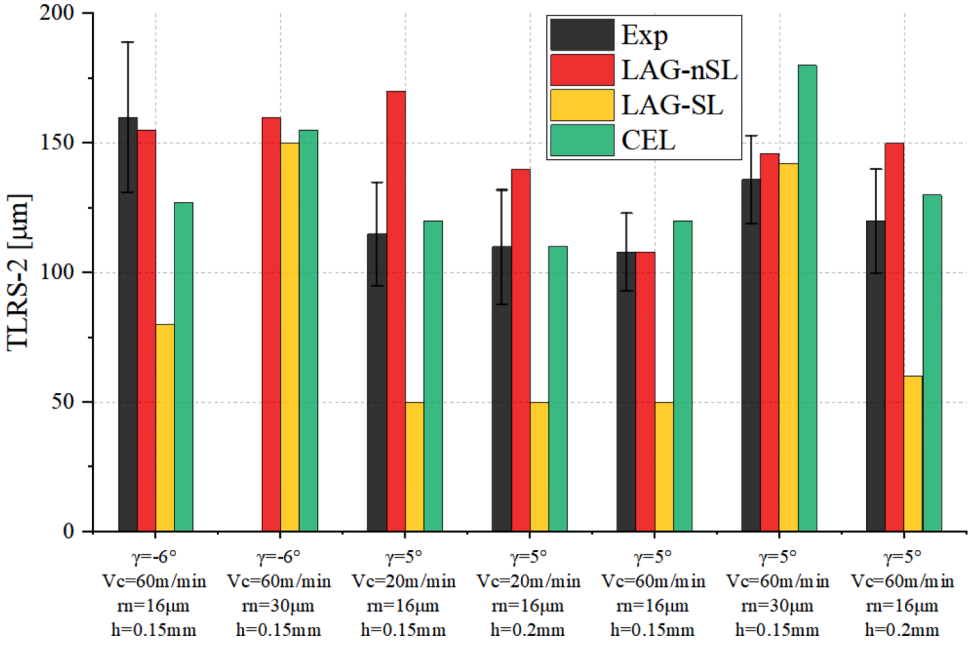


**Fig. 21.** Results of the depth of the RS affected layer in transversal direction (TLRS-2) from experiments and three simulation models.

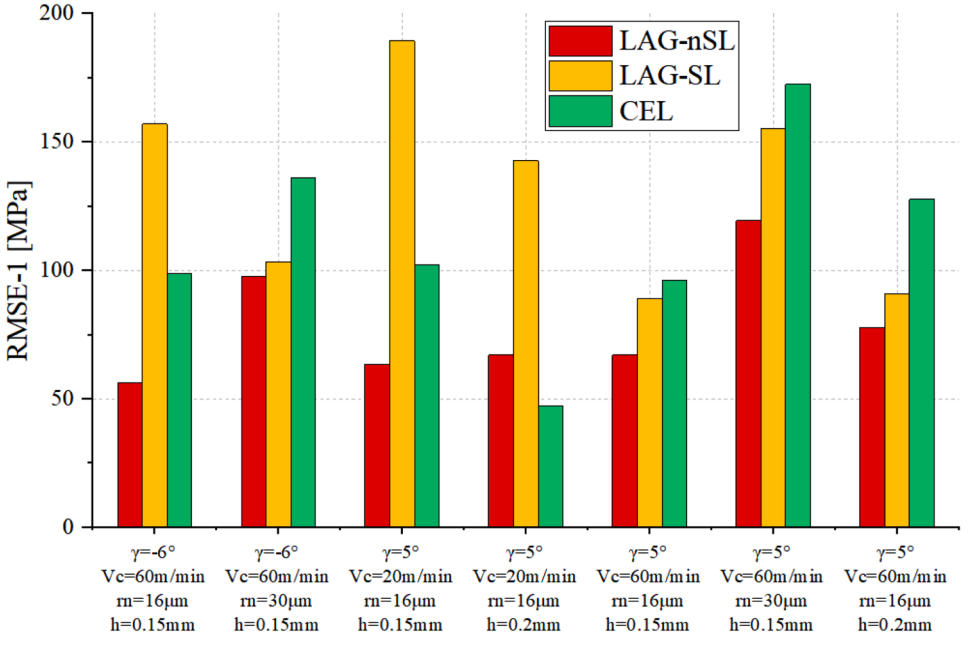


**Fig. 22.** Results of the root mean square error of RS curve in cutting direction (RMSE-1) from experiments and three simulation models.

## 6. Conclusions

In this paper, a comprehensive investigation is carried out on three numerical formulations used in machining simulation of Titanium alloy. In additional to the commonly used LAG-SL an CEL, an improved LAG-based model is proposed by removing SL (denoted by LAG-nSL) for wider applicability and better characterization of material flow in machining using tool with various edge micro-geometries. Correspondingly, three cutting models are developed with three formulations. The ability of these cutting models to simulate the cutting process is analyzed through comparisons between experimental and simulated results in terms of chip morphology, forces, and residual stresses. Table 4 summarizes the obtained results by showing the difference among these three

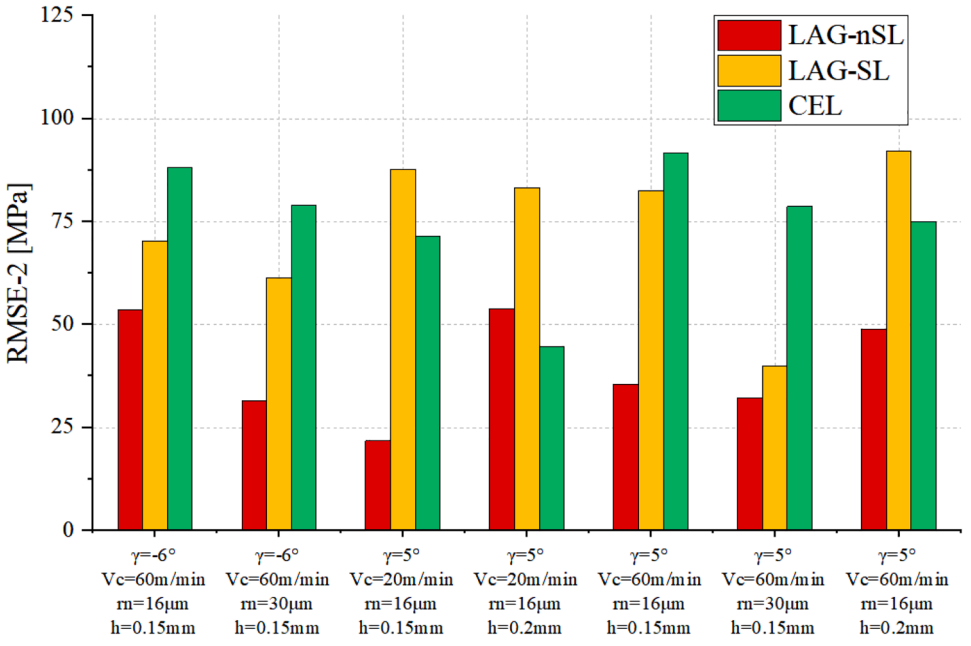


**Fig. 23.** Results of the root mean square error of RS curve in transversal direction (RMSE-2) from experiments and three simulation models.

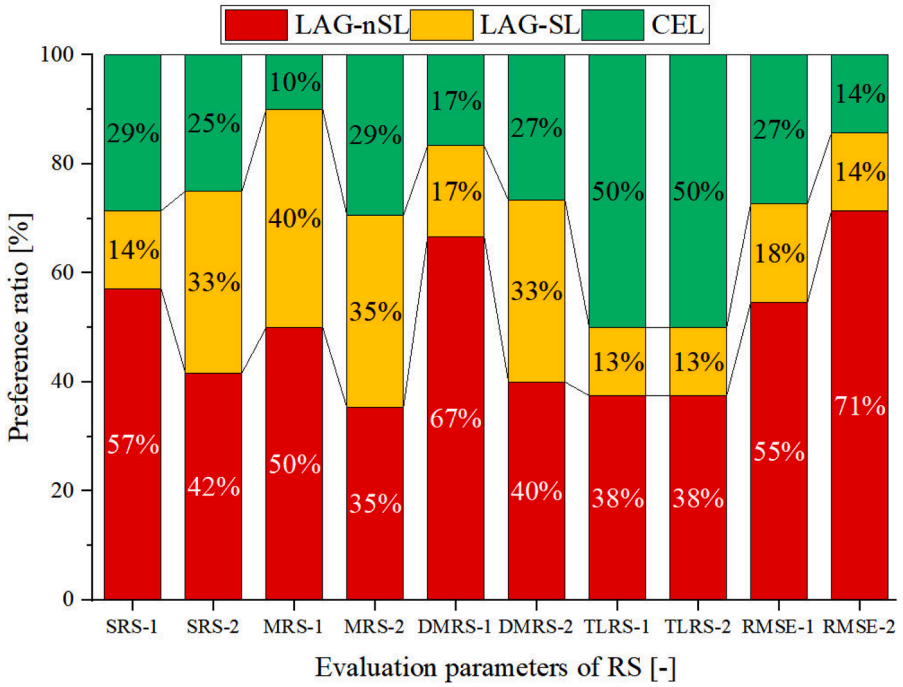


**Fig. 24.** Preference ratio of the three formulations in prediction of RS.

formulations.

As summarized in Table 4, the applicability of these three models in predicting forces and chip morphology is denoted by the prediction error. As for RS profile, the applicability is described by three levels: good, acceptable, and bad.

In case of the forces in cutting direction ($F_c$) and thrust direction ($F_t$), it reveals that the cutting model using LAG-nSL yielded the closet predictions in forces with an error of 12.8% in cutting direction and 9.3% in thrust direction. On the contrary, huge errors are noticed when using LAG-SL (30.8% in $F_c$ and 53.2% in $F_t$) and CEL (32.5% in $F_c$ and 42.3 in $F_t$). This means the interaction between tool

**Table 4**
Overall evaluation of cutting models using LAG-SL, LAG-nSL and CEL in terms of forces, chip morphology and RS profile. (+ +: good; +: acceptable: − is unacceptable).

| Model | Forces | | Chip morphology | | RS profile | | | | |
|---|---|---|---|---|---|---|---|---|---|
| | $F_c$ | $F_t$ | $CCR_m$ | $f_{seg}$ | SRS | MRS | DMRS | TLRS | RMSE |
| LAG-nSL | 12.8% | 9.3% | 9.5% | 48.5% | + + | ++ | ++ | + | ++ |
| LAG-SL | 30.8% | 53.2% | 16.9% | 50% | − | ++ | − | − | − |
| CEL | 32.5% | 42.3% | 20.3% | 137.7% | − | − | − | ++ | − |

cutting edge microgeometry and workpiece is severely underestimated in the presence of SL or Eulerian mesh.

As for the chip morphology, all those three models gave segmented chips. However, the one using CEL showed much overestimated segmentation frequency $f_{seg}$ (137.7%) than LAG-nSL (48.5%) and LAG-SL (50%). Besides, the cracks between chip segmentations were captured in both LAG-SL and LAG-nSL while not in CEL. It implies that an additional self-contact between elements is necessary to produce accurate chip morphology, which is however unavailable in CEL. The maximum chip compression ratio $CCR_{\mathrm{m}}$ is found better predicted by LAG-nSL than LAG-SL and CEL. It can be inferred from this finding that less material is flowing into chip when suing SL and Eulerian part once the cutting edge microgeometry is comparable to UCT.

In calculation of RS, the results from the cutting model using LAG-nSL showed good agreement with the experimental measurements of SRS, MRS, DMRS and RMSE, and acceptable agreement with those of TLRS. On the contrary, LAG-SL only showed good predictions in MRS while CEL in TLRS. This means that the deformation beneath tool cutting edge microgeometry is better simulated by removing SL from Lagrangian mesh.

## Data availability

Data will be made available on request.

## Acknowledgments

The authors would like to express their gratitude for the support from the National Natural Science Foundation of China (52175482), the State Scholarship Fund from China Scholarship Council (202106950032), the State Key Laboratory of Digital Manufacturing Equipment and Technology (DMETKF2021005), and the Laboratory of Materials and Processes (LaBoMaP) of Arts et Métiers Institute of Technology (ENSAM), which permitted to perform this research work.

## References

[1] H. Liu, X. Xu, J. Zhang, Z. Liu, Y. He, W. Zhao, Z. Liu, The state of the art for numerical simulations of the effect of the microstructure and its evolution in the metal-cutting processes, Int. J. Mach. Tools Manuf. 177 (2022), 103890.
[2] C. Hu, W. Zhang, K. Zhuang, J. Zhou, H. Ding, On the steady-state workpiece flow mechanism and force prediction considering piled-up effect and dead metal zone formation, J. Manuf. Sci. Eng. - Trans. ASME (2020) 143.
[3] C. Zhang, H. Choi, Study of segmented chip formation in cutting of high-strength lightweight alloys, Int. J. Adv. Manuf. Technol. 112 (2021) 2683–2703.
[4] K. Zhuang, J. Gao, T. Ye, X. Dai, Effect of cutting edge radius on cutting force and surface roughness in machining of Ti-6Al-4V, Proc. CIRP 108 (2022) 571–576.
[5] C. Hu, J. Wang, L. Lin, F. Lin, C. Fu, J. Outeiro, K. Zhuang, Effects of asymmetric passivation of tool cutting edge on microstructure evolution when cutting Inconel 718 alloy, Proc. CIRP 108 (2022) 141–146.
[6] Y. Liu, Numerical Investigation On the Formation Mechanism of Residual Stress in Metal Cutting, Lund University, 2021.
[7] V.P. Astakhov, Tribology of metal cutting, (2006).
[8] M. Lotfi, J. Akbari, Finite element simulation of ultrasonic-assisted machining: a review, Int. J. Adv. Manuf. Technol. 116 (2021) 2777–2796.
[9] C.H. Lauro, L.C. Brandão, S.L.M. Ribeiro Filho, R.A.F. Valente, J.P. Davim, Finite element method in machining processes: a review, in: J.P. Davim (Ed.), Modern Manufacturing Engineering, Springer International Publishing, Cham, 2015, pp. 65–97.
[10] A.U. Manual, Abaqus user manual, (2020).
[11] S. Deform-User Manual, Deform V10. 0.2, (2010).
[12] ThirdWaveSystems, Third Wave AdvantEdge TM User's Manual Version 7.3, (Third Wave Systems Vancouver, BC, Canada, 2017).
[13] H.A. Soliman, A.Y. Shash, T.M. El Hossainy, M. Abd-Rabou, Investigation of process parameters in orthogonal cutting using finite element approaches, Heliyon 6 (2020) e05498.
[14] Y. Zhang, J.C. Outeiro, T. Mabrouki, On the selection of Johnson–Cook constitutive model parameters for Ti-6Al-4V using three types of numerical models of orthogonal cutting, Proc. CIRP 31 (2015) 112–117.
[15] X. Xu, J. Outeiro, J. Zhang, B. Xu, W. Zhao, V. Astakhov, Machining simulation of Ti6Al4V using coupled Eulerian–Lagrangian approach and a constitutive model considering the state of stress, Simul. Model. Pract. Theory 110 (2021), 102312.
[16] M. Sadeghifar, R. Sedaghati, W. Jomaa, V. Songmene, A comprehensive review of finite element modeling of orthogonal machining process: chip formation and surface integrity predictions, Int. J. Adv. Manuf. Technol. 96 (2018) 3747–3791.
[17] F. Ducobu, E. Rivière-Lorphèvre, E. Filippi, Numerical contribution to the comprehension of saw-toothed Ti6Al4V chip formation in orthogonal cutting, Int. J. Mech. Sci. 81 (2014) 77–87.
[18] F. Ducobu, E. Rivière-Lorphèvre, E. Filippi, Material constitutive model and chip separation criterion influence on the modeling of Ti6Al4V machining with experimental validation in strictly orthogonal cutting condition, Int. J. Mech. Sci. 107 (2016) 136–149.
[19] D. Yameogo, B. Haddag, H. Makich, M. Nouari, A physical behavior model including dynamic recrystallization and damage mechanisms for cutting process simulation of the titanium alloy Ti-6Al-4V, Int. J. Adv. Manuf. Technol. 100 (2019) 333–347.
[20] W. Cheng, J.C. Outeiro, Modelling orthogonal cutting of Ti-6Al-4V titanium alloy using a constitutive model considering the state of stress, Int. J. Adv. Manuf. Technol. 119 (2022) 4329–4347.
[21] F.A.V. da Silva, J.C. Outeiro, Machining simulation of Inconel 718 using Lagrangian and coupled Eulerian–Lagrangian approaches, Proc. CIRP 102 (2021) 453–458.

[22] G. Rotella, D. Umbrello, Finite element modeling of microstructural changes in dry and cryogenic cutting of Ti6Al4V alloy, CIRP Ann. 63 (2014) 69–72.
[23] K. Zhuang, C. Fu, J. Weng, C. Hu, Cutting edge microgeometries in metal cutting: a review, Int. J. Adv. Manuf. Technol. 116 (2021) 2045–2092.
[24] F. Ducobu, E. Rivière-Lorphèvre, E. Filippi, Mesh influence in orthogonal cutting modelling with the coupled Eulerian–Lagrangian (CEL) method, Eur. J. Mech. - A/Solids 65 (2017) 324–335.
[25] Y. Bai, T. Wierzbicki, A new model of metal plasticity and fracture with pressure and lode dependence, Int. J. Plast. 24 (2008) 1071–1096.
[26] W. Cheng, J. Outeiro, J.-P. Costes, R. M'Saoubi, H. Karaouni, V. Astakhov, A constitutive model for Ti6Al4V considering the state of stress and strain rate effects, Mech. Mater. 137 (2019), 103103.
[27] M.R. Vaziri, M. Salimi, M. Mashayekhi, Evaluation of chip formation simulation models for material separation in the presence of damage models, Simul. Model. Pract. Theory 19 (2011) 718–733.
[28] M. Sima, T. Özel, Modified material constitutive models for serrated chip formation simulations and experimental validation in machining of titanium alloy Ti–6Al–4V, Int. J. Mach. Tools Manuf. 50 (2010) 943–960.
[29] L. Kops, M. Arenson, Determination of convective cooling conditions in turning, CIRP Ann. 48 (1999) 47–52.
[30] N.N. Zorev, Inter-relationship between shear processes occurring along tool face and shear plane in metal cutting, Int. Res. Prod. Eng. 49 (1963) 143–152.
[31] C. Courbon, F. Pusavec, F. Dumont, J. Rech, J. Kopac, Influence of cryogenic lubrication on the tribological properties of Ti6Al4V and Inconel 718 alloys under extreme contact conditions, Lubrication Sci. 26 (2014) 315–326.
[32] W. Cheng, Modelling of machining of Ti-6AI-4V titanium Alloy using a constitutive model accounting for the state of stress in the deformation zone, in: Ecole Nationale Supérieure d'arts et Métiers - ENSAM, 2019.
[33] E. Astm, Standard Guide For Preparation of Metallographic Specimens, ASTM International, 2011.
[34] Q. Yue, Y. He, Y. Li, S. Tian, Investigation on effects of single- and multiple-pass strategies on residual stress in machining Ti-6Al-4V alloy, J. Manuf. Process. 77 (2022) 272–281.
[35] J. Köhler, T. Grove, O. Maiß, B. Denkena, Residual stresses in milled titanium parts, Proc. CIRP 2 (2012) 79–82.
[36] S.Y. Liang, J.C. Su, Residual stress modeling in orthogonal machining, CIRP Ann. 56 (2007) 65–68.
[37] P. Niesłony, W. Grzesik, P. Laskowski, J. Sienawski, Numerical and experimental analysis of residual stresses generated in the machining of Ti6Al4V titanium alloy, Proc. CIRP 13 (2014) 78–83.
[38] Outeiro, J.C. "Residual stresses in machining." Mechanics of Materials in Modern Manufacturing Methods and Processing Techniques, 2020, pp. 297–360, https://doi.org/10.1016/B978-0-12-818232-1.00011-4.